Rotating Scan Strategy Induced Anisotropic Microstructural and Mechanical Behavior of Selective Laser Melted Materials and Their Reduction by Heat Treatments

Benedikt Diepold,* Mathias Sebastian Palm, Andreas Wimmer, Torsten Sebald, Heinz Werner Höppel, Steffen Neumeier, and Mathias Göken

Choosing a properly optimized rotating scan strategy during the selective laser melting (SLM) process is essential to reduce residual stresses and thus to obtain homogeneous properties. Surprisingly, anisotropic material properties are found in several materials that are built with the often applied rotating stripes scan strategy of Electro-Optical Systems (EOS) because the scan strategy avoids possible interactions of the laser beam with process by-products and therefore excludes a range of scanning directions. Herein, the alloys Hastelloy X, Inconel 718, and stainless steel 316L are investigated. Vertically built specimens with a cylindrical gauge geometry show an oval deformation during tensile testing, indicating a mechanical anisotropy in the horizontal x- and y-direction. Tensile tests along the x- and y-direction reveal a deviation of the yield strength of 7% for Hastelloy X. Analyses of the microstructures show differences in the grain morphology, size, and texture in all three coordinate planes of the three materials. This anisotropic behavior can be explained by a detailed study of the texture and the calculated Schmid factors. Heat treatments can reduce the textural and mechanical anisotropy due to recrystallization of grains but requires annealing at sufficiently high temperatures and long times.

B. Diepold, H. W. Höppel, S. Neumeier, M. Göken
Department of Materials Science & Engineering
Institute I: General Materials Properties
Friedrich-Alexander-Universität Erlangen-Nürnberg
Martensstraße 5, Erlangen 91052, Germany
E-mail: benedikt.diepold@fau.de

M. S. Palm, A. Wimmer
Institute for Machine Tools and Industrial Management
Technical University of Munich
Boltzmannstraße 15, Garching 85748, Germany

M. S. Palm, T. Sebald
ArianeGroup GmbH
Robert-Koch-Straße 1, Taufkirchen 82024, Germany

The ORCID identification number(s) for the author(s) of this article can be found under https://doi.org/10.1002/adem.202100622.

1. Introduction

The selective laser melting (SLM) process, also known as laser beam melting (LBM), is one of the most widespread additive manufacturing (AM) technologies. It enables the production and usage of parts with a high geometric accuracy and complexity combined with a low porosity.[1] Over the last decade many studies investigated in great detail the SLM processed materials. Earlier studies analyzed the influence of process parameters such as laser power, platform temperature, or scan strategy to improve the quality of the material, mainly with regard to the porosity.[2–6] More recent publications used state-of-the-art rotating scanning strategies and investigated the precipitation behavior of the investigated alloy[7,8] or the influence of the process on the grain structures and textures, often also in combination with heat treatments.[7]

It has been shown that the used scan strategy has an enormous influence on the melt pool geometry, grain morphology, grain size, and texture. An unidirectional scan pattern leads to a strong, nearly single-crystalline texture with long columnar grains in z-direction, due to the same temperature gradients over all layers of the part.[9,10] Rotating the scanning direction after each layer by 90° also leads to a special crystallographic orientation of grains and grain morphology due to the overlapping of each second layer.[11] Using a rotation by 67° avoids the same scanning direction in following layers. Such rotating scan strategies, which are often combined with scanning of random islands or stripes, have several advantages: after each layer, the direction of thermal gradients changes, resulting in lower and homogeneously distributed residual stresses,[12] which is necessary to avoid cracking in large parts.[13] In addition, the continuous change in the heat flux directions prevents the epitaxial growth of long columnar grains in distinct patterns.[10,14,15] Anisotropic effects are reduced due to a more homogenous texture among the two vertical coordinate planes xz and yz, but still remain in comparison with the horizontal plane xy.[16,17] Differences in grain morphology, grain size, texture, melt pool boundaries, and distribution of pores result in different mechanical properties in the vertical (z) and horizontal directions (x and y).[10,16,18–23] As there are no or just minor differences between both horizontal directions, most publications just

ADVANCED
SCIENCE NEWS

www.advancedsciencenews.com

**ADVANCED
ENGINEERING
MATERIALS**

www.aem-journal.com

separate between the horizontal and vertical plane. Only few publications investigated all three coordinate planes separately. Among these, the majority report no significant difference in the microstructure[11,20,24] and the mechanical properties[25] of the two vertical planes (xz and yz). Keshavarzkermani et al.[10] and Sun et al.[11] investigated Hastelloy X and a Ni–25 at% Mo alloy, which were processed on EOS M290 SLM machines with different scan strategies. Both reported isotropic microstructural properties in the xz- and yz-plane of the material processed with the scan rotation by 67°. However, the textures[10,11] and yield strengths (YS)[10] revealed small differences between the properties in x-direction (xz-plane) and y-direction (yz-plane). As the focus of their study was to highlight the textural and mechanical differences between three to four different scan strategies, the comparatively small deviations in x- and y-direction were neglected. This leads to the assumption that certain machine-dependent factors such as the direction of the inert gas flow can cause an x–y anisotropy, even though it is very small. It is well known that the rapid and local melting of the metal powder causes the formation of a welding plume of evaporated material, the ejection of spatter, and powder particles and severe interactions of the laser with these process by-products can occur.[26–31] Consequently, Reijonen et al.,[29] found that the laser can be attenuated while scanning in gas flow direction. Furthermore, they showed that the melt pool depth is sensible to the gas flow velocity because inadequate removal of process by-products causes an attenuation of the laser beam. In addition, Andreau et al.[31] investigated the melt pool shape and grain structure of samples, which were produced with the same processing parameters using a meander-like, bidirectional scanning strategy. The sample whose scan pattern was aligned parallel to the gas flow had a 33% reduced melt pool depth in comparison with the sample whose scan pattern was aligned perpendicularly to the gas flow. In addition, the grain structure in the corresponding planes (transversal to the scan direction) was different. They concluded that a better control of the vapor plume by the gas flow would be beneficial for homogenous material properties. As the gas flow velocity is limited due to the pick-up of powder, another possibility to avoid a possible attenuation of the laser is to omit certain scan angles.

Accordingly, the current work investigates the properties of different materials that were produced using a 67° rotating stripe scan strategy, where angles that may cause interactions of the laser with process by-products were left out. Therefore, stainless steel 316L and two nickel-base superalloys, Hastelloy X (HX) and Inconel 718 (IN718), were produced on an EOS M290 SLM machine using the latest standard scanning strategy provided by the manufacturer. Tensile tests and electron backscatter diffraction (EBSD) measurements were conducted to study whether this scan strategy leads to isotropic or still anisotropic properties by analyzing the deformation behavior and microstructures. Detailed investigations were conducted for Hastelloy X. In addition, the effect of heat treatments on the anisotropy of three different alloys was identified.

2. Experimental Section

2.1. Manufacturing of the Samples

The manufacturing of the three different materials was performed on different EOS M290 (EOS GmbH, Krailling,

Germany) SLM machines. The machines were equipped with the additional system EOSTATE Exposure OT, which monitors the entire built process. This equipment was developed by MTU Aero Engines AG.[32] Standard process parameters "HX_PerformanceM291 2.12" were used for the manufacturing process of Hastelloy X. Identical parameters were used for IN718 and 316L. The powder supplier, particle size, energy density, layer thickness, and spot size of all three alloys are shown in **Table 1**. The energy density was calculated by dividing the laser power through the product of scan speed and hatch distance according to the equation of Song et al.[33] The laser spot size is 100 μm. The chemical composition of all three materials in accordance with the data sheets of the powder suppliers is shown in **Table 2**. The HX powder fulfills the requirements of the European standards NiCr22Fe18Mo, 2.3665 and the US standard UNS N06002. The chemical composition of 316L corresponds to the ASTM F138 material standard for surgical implants and that of IN718 to AMS 5662 bar material. The arrangement and geometry the parts are shown in **Figure 1**a,b exemplarily for Hastelloy X. Two cuboids ($90 \times 50 \times 12 \, mm^3$) were placed with their long side either along the x- or y-direction. In addition, several vertical cylinders with a diameter of 10 mm were manufactured. The built job also contained the manufacturing of samples that were not used in this study.

2.2. Conditions and Heat Treatments

Depending on the alloy, different heat treatment procedures after the additive manufacturing are necessary to reduce residual stresses, homogenize the material, or precipitate strengthening phases. In the case of Hastelloy X, two different heat treatments were conducted in an electrical vacuum furnace (Nabertherm, Lilienthal, Germany). The so-called condition HX-1177 was heat-treated at a maximum temperature of 1177 °C for a holding time of 12 min. The HX-1200 specimens were held at 1200 °C for 4 h. In both conditions, the samples were cooled down in the vacuum furnace with a maximum rate of 5 K min^{-1}. The 316L material was subjected to a heat treatment with a maximum temperature of 1050 °C for 1 h. The heat treatment procedure of IN718 consisted of a stress relief annealing at 960 °C for 1 h, a subsequent solution heat treatment at 960 °C for another 1 h and a two-stage ageing treatment with the first stage at 760 °C for 5 h and the second stage at 650 °C for 1 h. **Table 3** shows the labeling and conducted heat treatments of all investigated conditions.

Table 1. Applied SLM process parameter for Hastelloy X, IN718, and 316L.

Alloy	Powder supplier	Powder particle size [μm]	Energy density [J mm^{-2}]	Layer thickness [μm]	Spot size [μm]
HX	Aubert&Duval	10–54	2.7	40	100
IN718	Oerlikon	15–45	2.7	40	100
316L	EOS	20–65	2.7	40	100

**ADVANCED
SCIENCE NEWS**

www.advancedsciencenews.com

**ADVANCED
ENGINEERING
MATERIALS**

www.aem-journal.com

Table 2. Chemical composition of Hastelloy X, IN718, and 316L in wt% in accordance with the data sheets of the corresponding suppliers.

HX	Ni	Cr	Fe	Mo	Co	W	Mn, Si	Al, Cu	Ti	C	S, O, N	P	B
min.	bal.	20.5	17	8	0.5	0.2	–	–	–	–	–	–	–
max.	bal.	23	20	10	2.5	1.0	1.0	0.5	0.15	0.1	0.03	0.04	0.01
IN718	Ni	Cr	Fe	Mo	Nb+Ta	Al	Ti						
	bal.	18	18	3	5	0.6	1						
316L	Ni	Cr	Fe	Mo	C	N							
min.	13	17	bal.	2.25	–	–							
max.	15	19	bal.	3	0.03	0.1							
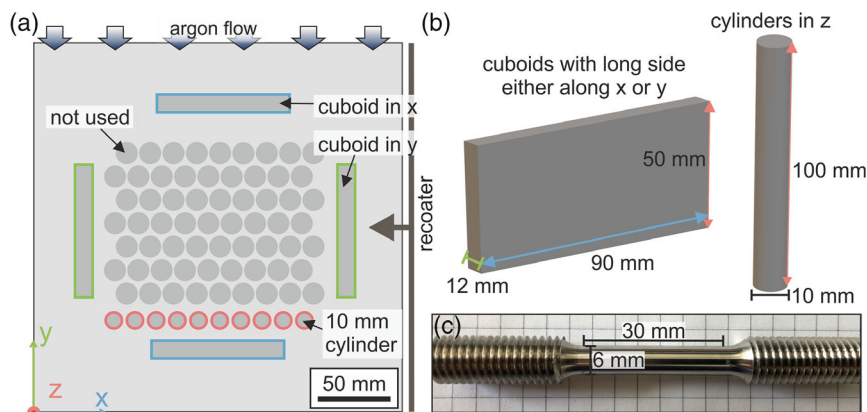
Figure 1. a) Arrangement of Hastelloy X samples on the building platform. Tensile specimens were machined out of cuboids along the *x*-direction (blue), cuboids along the *y*-direction (green), and cylinders in *z*-direction (red). b) 3D view and dimensioning of the built sample geometries. c) Photograph of a tensile test specimen.

Table 3. Labeling and heat treatment procedure of investigated conditions.

| Alloy	Labeling of condition	Heat treatment procedure
Hastelloy X	HX-ab	No heat treatment/as-built condition
Hastelloy X	HX-1177	$T_{max} = 1177\,°C$ for 12 min
Hastelloy X	HX-1200	$T_{max} = 1200\,°C$ for 4 h
IN718	IN718-ab	No heat treatment/as-built condition
IN718	IN718-960	Stress relieve annealing (SRA) at 960 °C for 1 h + solution annealing (SA) at 960 °C for 1 h + age at 760 °C for 5 h and 650 °C for 1 h
316L	316L-1050	$T_{max} = 1050\,°C$ for 1 h

2.3. Specimen Preparation and Characterization

Specimens for microstructural investigations were ground to a grit size of 2500 and mechanically polished using a 3 µm diamond suspension with succeeding electrochemical polishing in an electrolyte A3 (Struers GmbH, Willich, Germany). For the investigation of melt pool boundaries by optical microscopy, specimens were etched electrochemically in Kalling's 2 reagent. Microstructural analyses were conducted on a scanning electron microscope (SEM) Zeiss Crossbeam 540 with an attached back scattered electron (BSE) detector, scanning transmission electron microscopy (STEM) detector, Oxford Nordlys 2 EBSD detector, and energy-dispersive X-ray spectroscopy (EDS) detector. The HKL Channel 5 software package was used for postprocessing of the EBSD data. Low-angle grain boundaries (LAGB) were defined for angles between 2 and 15° and appear as fine black lines, and high-angle grain boundaries (HAGB) with angles >15° appear as thicker black lines in the EBSD maps. Local misorientation mappings were created for a filter size of 3 × 3. The fraction of recrystallized grains of heat-treated Hastelloy X was also analyzed using the EBSD software.

2.4. Tensile Tests

Tensile tests were conducted along the *x*-, *y*-, and z-direction in regard to the SLM coordinate system (see Figure 1a). Therefore,
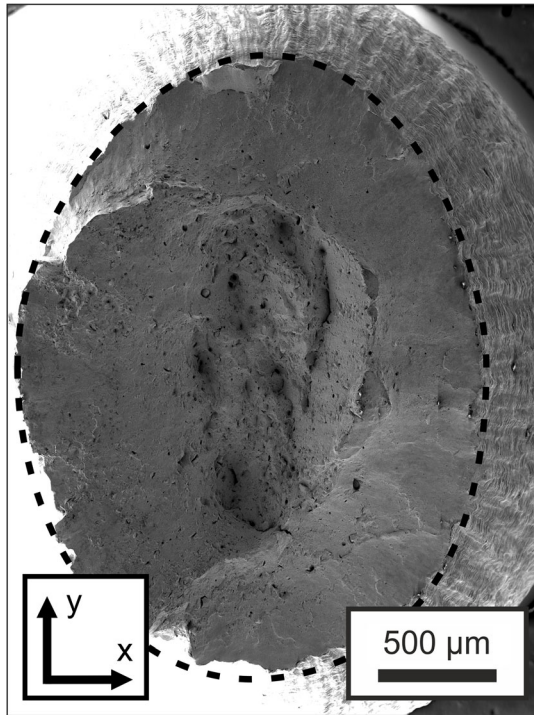
Figure 2. SEM image of the fracture surface of a HX-ab tensile specimen. All investigated SLM samples contract more in x-direction than in y-direction during tensile testing in z-direction.

cylinders with a diameter of 10 mm were machined by electric discharge machining out of SLM cuboids, which were aligned either along the x- or y-direction. These rods as well as the manufactured cylinders in z-direction were turned to cylindrical M10 tensile specimens with a gauge length of 30 mm and a diameter of 6 mm in accordance with DIN EN 50125 (see Figure 1c). The tests were conducted on an Instron 4505 testing machine equipped with a 100 kN load cell and a clip-on extensometer. The strain rate of all tests was $10^{-3}\,s^{-1}$. After tensile testing, the cross section of the specimens, which were built in z-direction, was asymmetric. Thus, the diameter in x-direction d_x and in y-direction d_y was measured around 10 mm away from the fracture surface using a digital micrometer. Exemplarily, a SEM image of the HX-ab condition is shown in **Figure 2**. In all cases, the x-direction contracted more than the y-direction. The ovality O was determined as the ratio of d_x to d_y according to Equation (1). In addition, the ratio of transversal to axial strain ν_x and ν_y was determined for the x- and y-direction according to Equation (2). The averaged properties of the oval cross section were obtained from three specimens per material and condition. A minimum of two specimens were used to determine each average values of the x- and y-direction of the as-built and HX-1177 condition of Hastelloy X. For the HX-1200 condition, only one test per direction was conducted. Tensile tests of IN718 and 316L were only conducted in the z-direction.

$$O = \frac{d_x}{d_y} \tag{1}$$

$$\nu_x = \frac{d_x/D}{e_f}; \nu_y = \frac{d_y/D}{e_f} \tag{2}$$

where d_x and d_y are the diameters after fracture in x- and y-direction, ν_x and ν_y are the ratios of transversal to axial strain in x- and y-direction, D is the gauge diameter before fracture, and e_f is the strain at fracture.
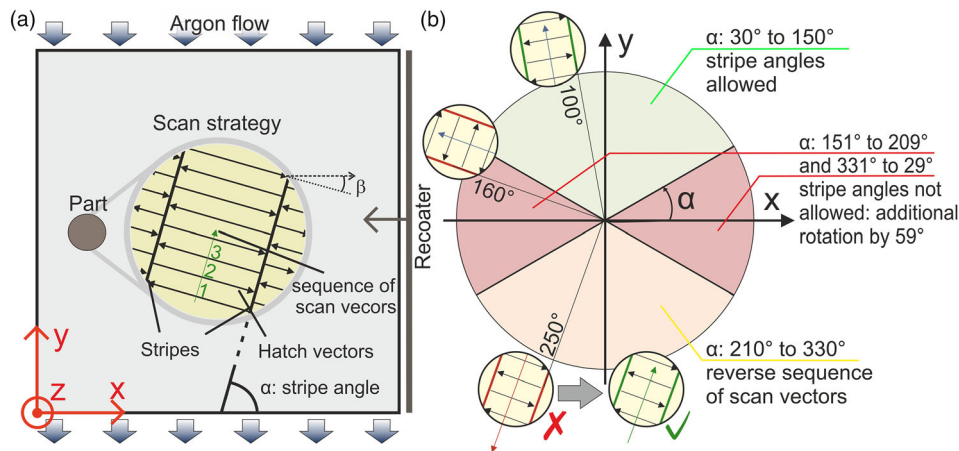
3. Scan Strategy

The manufacturing of samples was conducted on an EOS M 290 using the latest standard rotating stripe scan strategy provided by EOS. As the complex systematic of the scan strategy, included in the parameter set "HX_PerformanceM291 2.12," is not reported in the literature, it was reconstructed by the observation of the stripes in the EOSTATE Exposure OT tool.[32] It revealed that this industrial scan strategy is not just simply rotating by a certain angle. The whole platform is sectioned for each layer into stripes with 10 mm, which have a certain stripe angle α to the x-axis. These stripes are filled with perpendicular, alternating forward and backward scan vectors, which are exposed by the laser. After each layer, the whole stripe pattern and the including scan vectors are rotated by an angle of 67°. However, certain stripe angles are left out, as shown in **Figure 3**b. Only the angular region between 30 and 150° (green zone) is used. The exposure sequence of the scan vectors is reversed in stripes with angles between 210 and 330° (orange zone). If the calculated stripe angle is between 331 and 29° as well as between 151 and 209°, further 59° is added. This systematic recipe avoids the interaction or attenuation of the laser beam with by-products as the argon gas flow transports these by-products counters the y-axis (compare Figure 3a).[26]

Alternating scan vectors are embedded within the stripes, perpendicularly to the stripe direction. Thus, the scan vector angles β range from −60 to 60° to the x-axis, which means that no exposure occurs in a range of ± 30° to the y-direction. The effect of a hypothetic exposure along two distinct angles, $\beta = 0°$ and $\beta = -60°$, on the melt pool structure is shown schematically in **Figure 4**a,b. Optical microscopy reveals the real anisotropic melt pool structure, exemplarily shown for etched samples of Hastelloy X in Figure 4c. As it can be seen, the melt pool tracks are cut longitudinally (Figure 4c, label 1) and transversally in the xz-plane. In the yz-plane, melt pool tracks are cut only transversally (Figure 4c, arrow 2). This is due to the angular limitation of the scan vectors to only ± 60° to the x-axis in this EOS standard rotating stripe scan strategy.
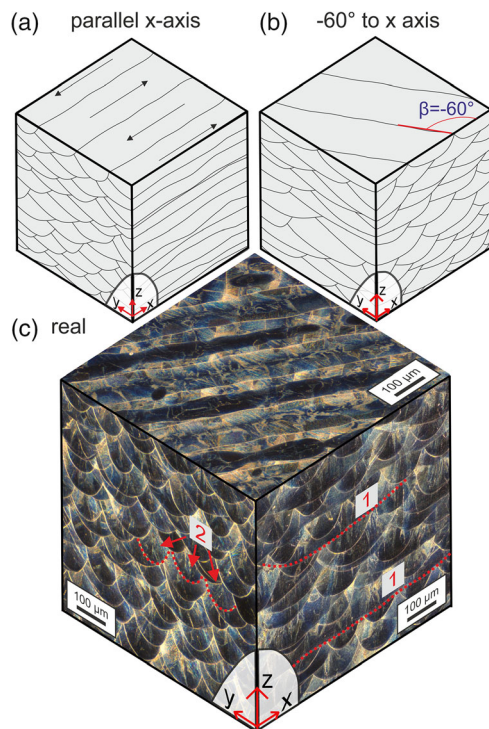
4. Results

4.1. Anisotropic Microstructures of the Alloys Hastelloy X, IN718, and 316L and Their Deformation Behavior

EBSD measurements revealed an anisotropic grain structure and texture in the three coordinate planes (see **Figure 5**). All three investigated additively manufactured materials show a stripe pattern perpendicular to the building direction (xy-plane), which is a result of the melt pool width and the rotation after each layer. This is similar to the bimodal diamond pattern, which results from an island scan strategy.[34] In contrast to the diamond pattern,[34] the inner cell grains of the stripes in the xy-plane exhibit a strong texture in <101> direction. In the case of IN718-ab, a

Figure 3. a) Definition of the coordinate system, directions of the gas flow and the recoating system as well as the visualization of the rotating stripes scanning strategy of the additive manufacturing process. b) Illustration of the allowed stripe angles α of the scan strategy: after each layer, the stripes and the embedded scan vectors are rotated by $67°$. If the resulting angle is in the red or orange angular region, further rotations are applied.


Figure 4. a) Schematic illustration of the resulting shape of melt pool boundaries after bidirectional scanning parallel to the x-axis and b) bidirectional scanning along the limit angle $\beta = -60°$. c) The real melt pool morphology obtained from etched samples. The melt pool structure is a composition of bidirectional scanning in the angular region from $-60°$ to $60°$ with respect to the x-axis. Melt pools are cut transversally and longitudinally in the xz-plane and only transversally in the yz-plane.

high amount of <001> textured grains surround these inner cells. As both Ni-base superalloys were manufactured with the identical energy input, either the complex precipitation behavior of IN718 or the different powder particle size distribution may cause its finer and differently textured grain structure. The 316L-1050 condition exhibits a grain structure, which is more like the grain structure of HX-ab, although that material was heat-treated. All three materials reveal differences between the xz- and yz-plane. The xz-plane exhibits an elongated and the yz-plane a V- or U-shaped grain morphology. In addition, the textures of the two vertical coordinate planes are different, indicated by the inverse pole figure (IPF) coloring.

The origin of the texture and grain shape can be found in the dendritic solidification along the highest temperature gradient, which is mostly directed toward the center of the melt pool tracks.[35–38] EBSD measurements with high magnification on etched samples show the melt pool structure as well as the grain structure (**Figure 6**). As the melt pool is narrow in transversal direction and quite long in longitudinal direction, the temperature gradients longitudinal to the melt track are by far lower compared with the transversal direction.[37] This leads to irregular grain shapes, if a melt track is cut longitudinally (Figure 6a, label 1 and 2). Some grains grew from a previous layer to the next (1), forming large, elongated grains, while others are quite small (2). This results in a bimodal grain size distribution of larger elongated grains and equiaxed grains in this layer. In contrast, the yz-plane shows quite regularly V-shaped grains (see Figure 6b), as the dendrites and grains grew mostly toward the center of the melt pools. This behavior is very dominant for a nonrotating bidirectional scan strategy in x-direction, as it is also shown by Andreau et al.[31]

The microstructural anisotropy also affects the mechanical properties. Tensile tests in z-direction were conducted for all three SLM materials in the as-built (only Hastelloy X, IN718) and heat-treated conditions. All vertically built and pulled specimens exhibit an oval cross section over the whole gauge length after the tensile tests which do not occur in conventionally cast and wrought materials. This means that the material contracts in x-direction more strongly than in y-direction, which is exemplarily shown by the fracture surface of an as-built Hastelloy X specimen in Figure 2. The geometric analysis of the cross sections in **Figure 7** shows a different degree of ovality for the various
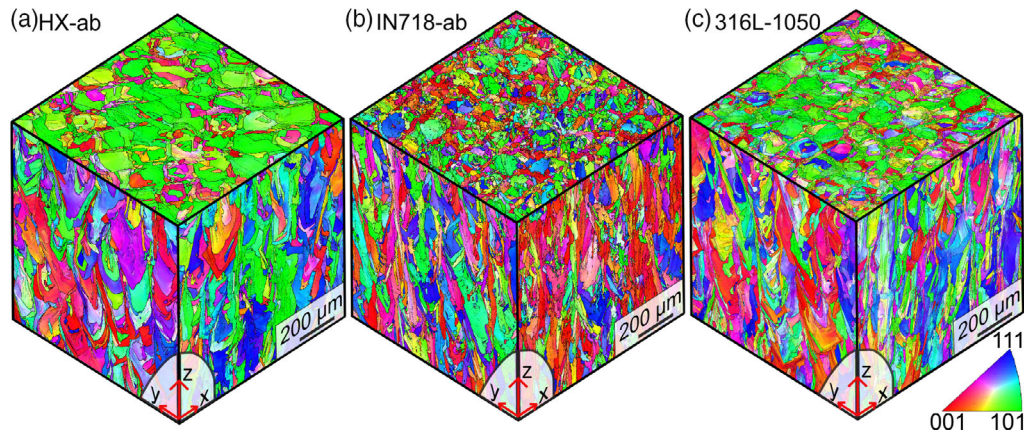
Figure 5. 3D illustration of grain orientation mappings of the three coordinate planes of a) as-built Hastelloy X, b) as-built IN718, and c) heat-treated 316L. All three materials exhibit an omnidirectional anisotropy regarding the grain morphology and texture.
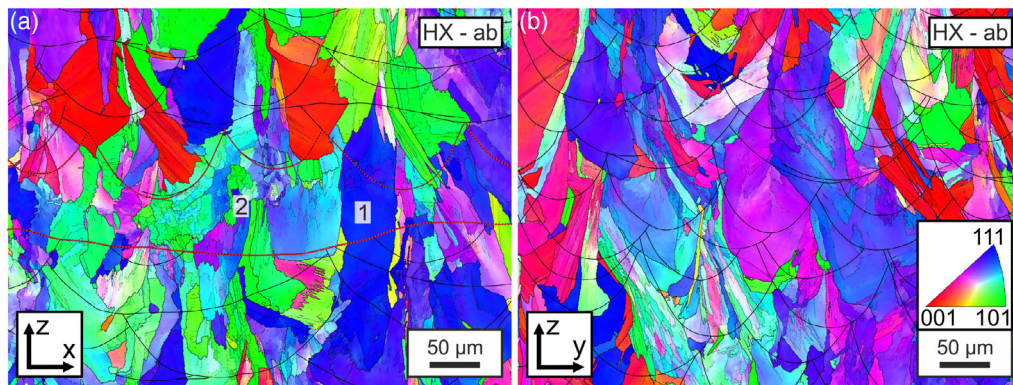
Figure 6. EBSD images of the a) xz-plane and b) yz-plane showing the relationship of melt pool boundaries (overlaid lines) and grain structure. Grains solidified either as columnar (1) or as small equiaxed grains (2) in longitudinally cut melt pools of the xz-plane. Grains in narrow melt pools (primarily in the yz-plane) grew tilted toward the center of the melt pool.
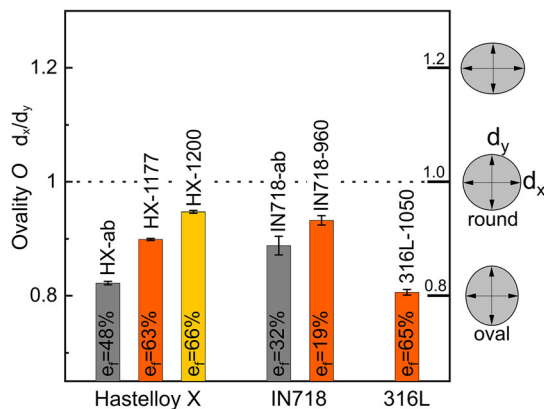

Figure 7. Ovality of Hastelloy X, IN718, and 316L in the as-built and heat-treated conditions. The percentages given in the bars represent the average elongation to fracture e_f.

materials and conditions. In the case of Hastelloy X, the ratio of diameters increased from 0.82 (HX-ab) to 0.95 (HX-1200), which means that the deformation induced geometrical anisotropy is reduced due to the conducted heat treatments. The heat treatments on IN718 also lead to lower ovalities of the cross sections. However, heat-treated 316L exhibits the highest ovality in comparison with the two Ni-base superalloys. This could be a result of the much larger average strain to fracture of the 316L specimens (Figure 7b).

4.2. Detailed Microstructural Characterization of Hastelloy X in the As-Built Condition

The microstructure on the microscale consists of dendritic structures in the as-built condition. The growth direction of the dendrites was determined by the temperature gradient during the SLM process. **Figure 8**a shows the dendritic structures of one melt pool in the xz-plane. It should be noted that the melt pool structure is different in all coordinate planes due to the scan strategy (see Figure 4), but the dendrites in the interior of melt pools are similar. Many columnar dendrites grew toward the melt pool interior and were therefore cut longitudinally in the xz-plane (Figure 4, label 1). In addition, there are some regions, mostly in the upper outer part of melt pools, where the columnar dendrites are tilted and cut in a cellular shape (2). This cellular shape could be also an indication for an equiaxed dendritic growth;
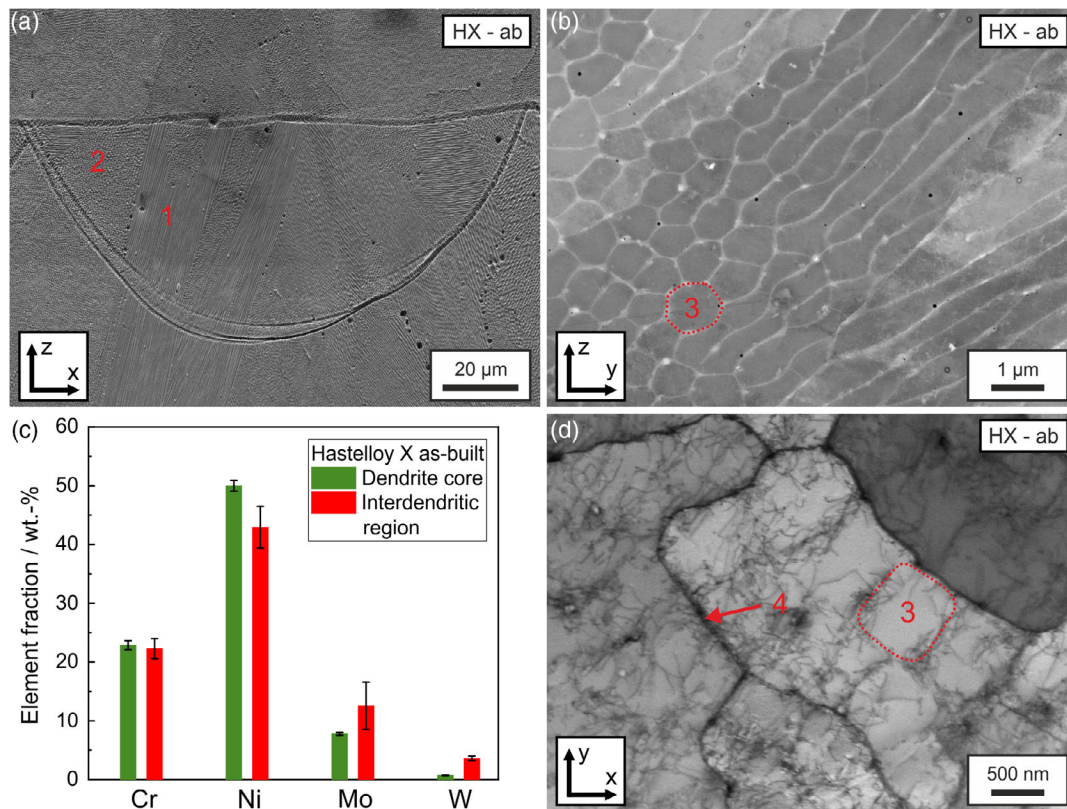
Figure 8. Microstructural investigation of as-built Hastelloy X: a) SE image of an etched sample shows columnar (1) and cellular regions (2). b) BSE image at a high magnification shows the dendritic substructure. c) Chemical composition of the dendrite core and the interdendritic region including segregations determined by EDS point measurements. d) STEM image showing entangled dislocations in the interdendritic regions (3) and subgrains (4).

however, it is reported that this occurs only at the upper part of a melt pool, due to remelting during the manufacturing of the next layers.[37,39] Both regions can be seen at higher magnifications in Figure 8b. The cellular and columnar appearance of the dendrites is detected in all three coordinate planes. As the dendrites grew mostly along the building direction, the planes parallel to the building direction (xz and yz) exhibit more columnar regions in comparison with the xy-plane. The BSE contrast revealed the segregation of heavier elements at the boundaries of the dendrites as these interdendritic regions appear bright. EDS point analysis (Figure 8c) confirmed an enrichment of Mo and W. The diameter of the cells was determined to be around 0.7 μm. STEM investigations (Figure 8d) revealed a high dislocation density. The dislocations are heavily entangled in the interdendritic regions, forming the cellular (3) and columnar network. In addition, many subgrain boundaries (4) can be seen.

EBSD mappings of the as-built condition were recorded to analyze the grain morphology and orientation. The mappings of each coordinate plane are shown in **Figure 9**. In the xy-plane, a checkered pattern can be detected. Large <101> orientated grains with a diameter of about 100 μm are surrounded by smaller <001> oriented grains. As described in section 4.1, the complex scan strategy causes different textures in the xz- and yz-plane. In the xz-plane, columnar grains with a preferred <111> and <101> orientation are predominant, whereas more

crescent-shaped grains can be found in the yz-plane. Each coordinate plane shows different frequencies of orientations, which can be derived from a comparison of the contour plots in Figure 9d. The <101> orientation in the xy-plane is around five times higher in comparison with a uniform distribution.

4.3. Influence of Heat Treatments

Heat treatments performed at a maximum temperature of 1177 °C (HX-1177) and 1200 °C (HX-1200) lead to a nearly complete dissolution of the fine interdendritic segregations and thus to a homogenization of the material on the microscale. However, substructures (arrow 1) can be found in the remaining unrecrystallized grains (arrow 2) (see **Figure 10**). The reduction of segregations in these regions and the complete absence of segregations in recrystallized grains go along with the reduction of the overall dislocation density because dislocations are primarily located at the cell boundaries in the as-built condition.[18] The fraction of recrystallized grains is around 90% in the HX-1177 condition and around 94% in the HX-1200 condition. Both heat treatments cause the formation carbides. In the case of HX-1177, low amounts of carbides were formed at the grain boundaries with a length of up to 1 μm (see Figure 10a).[18,40] In contrast, a higher fraction of coarser carbides is precipitated during the HX-1200 heat treatment.
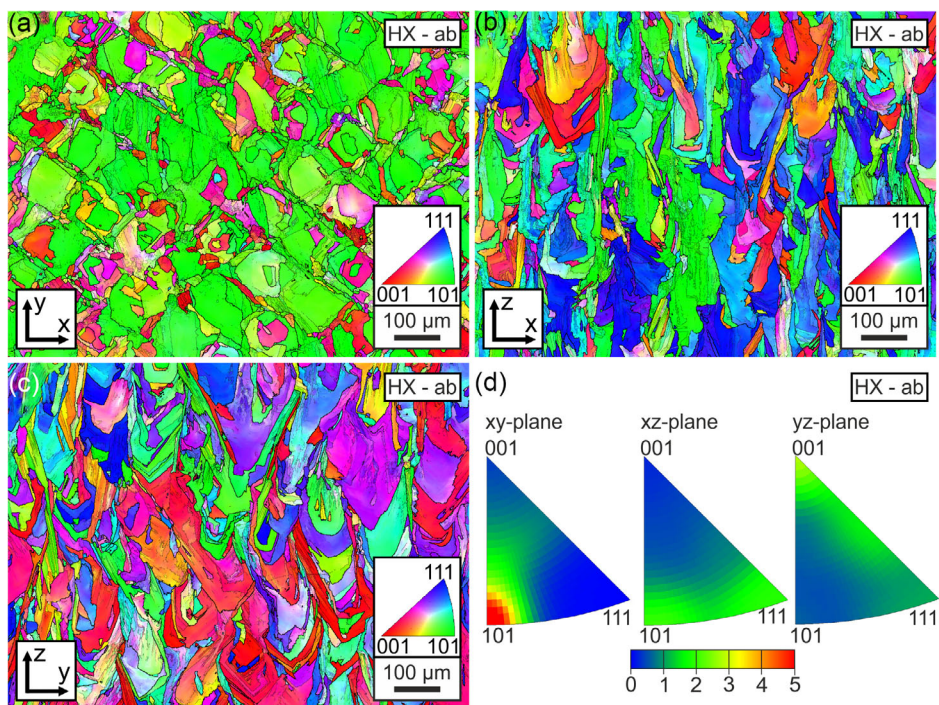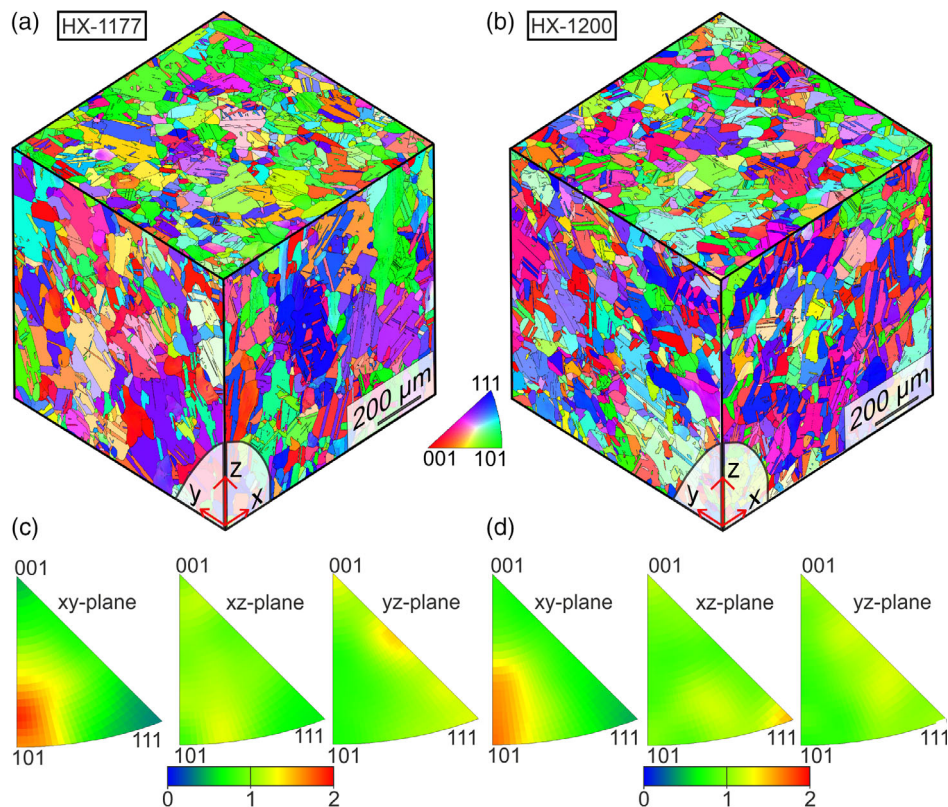
Figure 9. EBSD analyses of the three coordinate planes of Hastelloy X in the as-built condition. a) The *xy*-plane shows lines of grains aligned along scan vectors. b) *xz*-plane exhibits elongated grains in *z*-direction. c) The *yz*-plane shows crescent-shaped grains. d) Multiples of a uniform distribution of the three coordinate planes show a strong <101> texture in the *xy*-plane, a medium texture along the <101> and <111> direction in the *xz*-plane, and a slight texture along the <001> direction and toward <111> tilted direction in the *yz*-plane.
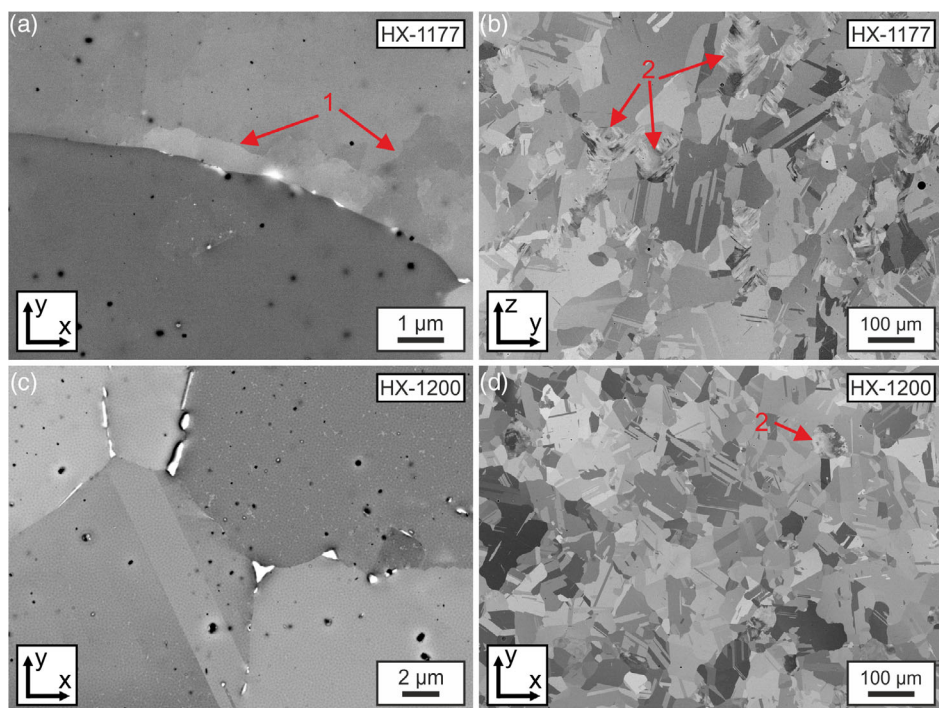
Figure 10. BSE images of the microstructure of heat-treated Hastelloy X in the a,b) HX-1177 and c,d) HX-1200 condition show a high fraction of recrystallization. Substructures (1) can be found in remaining unrecrystallized grains (2). In the HX-1200 condition, coarser carbides were formed (c) and a higher amount of recrystallization was achieved.

Figure 11. 3D view of the grain orientation mappings of the three coordinate planes of the a) HX-1177 and b) HX-1200 condition with their corresponding texture distributions in c) and d).

The orientation and morphology of the grains changed during the heat treatments due to recrystallization (see **Figure 11**). The small grains around the former <101> oriented larger grains in the middle of the stripes as well as the whole stripe pattern disappeared in the *xy*-plane. The former strong texture along the <101> direction almost vanished. The maximum multiple of uniform distribution was reduced from around 6 in the as-built condition to around 2. The recrystallized grains have a polygonal shape with straight grain boundaries in all three planes. The grains in the *xz*-plane recrystallized during the heat treatment of the HX-1177 condition in an elongated shape, whereas the grains seem to have a larger width in the *yz*-direction, which results from the former V-shaped morphology. Slight differences in the distribution of orientations are still detectable among these two planes (Figure 11c). The higher temperature and holding time of the heat treatment of the HX-1200 condition led to a more equiaxed polygonal grain shape in the *xz*- and *yz*-plane. The textural differences between the planes are further reduced.

4.4. Anisotropic Tensile Properties

The microstructural differences in the three coordinate planes indicate that the mechanical properties are also different in each direction. Results of tensile tests in each direction are shown in **Figure 12**. The ultimate tensile strength (UTS) of HX-ab is the highest in the *y*-direction (799 ± 1 MPa) and the lowest in the *z*-direction (661 ± 3 MPa). The UTS of the *x*-direction is similar to

the *y*-direction. However, regarding the YS, there is also a difference between *x*- and *y*-direction of 44 MPa. Annealing at 1177 °C for 12 min leads to a reduction of the anisotropy and to a significant reduction of the YS. Slight differences between the three directions could be still found in the work hardening behavior, resulting also in a deviation of the average elongation to fracture. The ductility in all directions is further increased after the heat treatment of the HX-1200 condition, while the anisotropy is further reduced. The YS in *x*-, *y*-, and *z*-direction amounts to 302, 303, and 290 MPa, respectively.

5. Discussion

The used complex rotating scan strategy allows only scanning in an angular region ± 60° perpendicular to gas flow direction to increase the processing stability. Thus, process by-products are removed out of the processing zone and no attenuation of the laser can occur. However, this goes along with a slightly anisotropic microstructure. In the following, we explain how this affects the mechanical properties of the as-built conditions of Hastelloy X, 316L, and IN718 and how subsequent heat treatments alter the anisotropy. In the future, the development and application of real-time melt pool monitoring systems may be able to modulate processing parameters by a feedback signal,[41] such that a stable process and isotropic properties can be obtained.
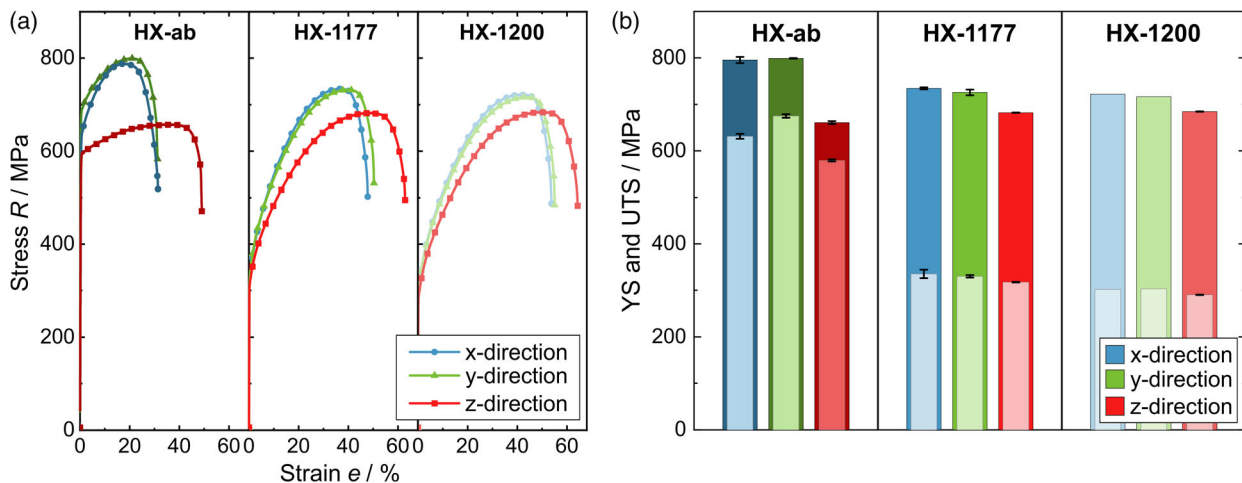
Figure 12. Tensile properties of Hastelloy X in the HX-ab, HX-1177, and HX-1200 condition. a) The stress–strain curves of samples pulled along the three coordinate axis and b) the average YS and UTS of all three conditions. The stress–strain behavior shows anisotropic properties in the as-built condition, a reduced anisotropy in the HX-1177 condition and an almost homogeneous behavior in the HX-1200 condition.
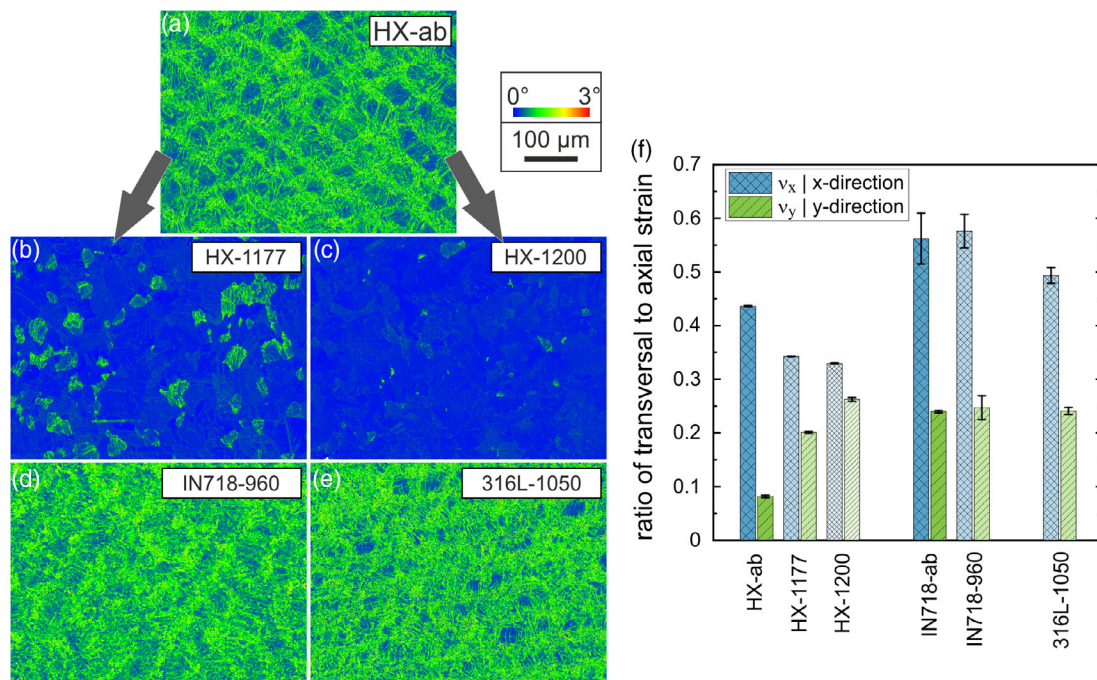
5.1. Microstructural Influence on the Anisotropic Mechanical Properties

The scan strategy induced anisotropy leads to a 7% lower YS in the *x*-direction and a 14% lower YS in the *z*-direction compared with the *y*-direction. In addition, the *z*-direction exhibits a lower strain hardening and thus a far lower ultimate tensile strength. There are different approaches to explain these differences. First, differences between the horizontal and the vertical plane can result from the solidification direction and the shape of melt pools. The melt pool boundaries form sharp angles in the conjunction of two adjacent melt pools in the vertical planes (compare Figure 8c,d). These may act as crack initiation sites under tensile loading.[18,42–44] Also, Tang et al.[19] detected the tearing along the softer, coarser dendritic cell region at the melt pool boundaries in fractured tensile samples.[19] Second, the grain shape has an influence on the mechanical properties because the grain boundaries act as dislocation barriers or preferred paths for crack propagation. The lower ductility in the horizontal directions could be a result of the orientation of the columnar grains. In that orientation, the short side of the columnar grains is parallel to the tensile stress axis, and the long side is perpendicular to it. This means that cracks can propagate in the easy mode 1 type along the long grain boundaries resulting in a lower ductility, which was proven for the horizontal plane.[16,22] Third, the varying textures lead to different mechanical properties. It is well known that the Young's modulus of Ni-base superalloys is anisotropic, which also affects the tensile properties of textured, additively manufactured materials.[20] Furthermore, and most important, the resolved shear stress on the favorable glide system depends on the orientation of each grain. Ni et al.[16] investigated the as-built condition of Ni-base superalloy IN718 and calculated the Schmid factors of the {111}<110> slip system.[16,22] They found a reduction of the Schmid factor if stresses are applied horizontally which explains the higher strength of horizontal specimens. An analogous behavior was found in this investigation. **Figure 13** shows the cumulated probability of Schmid
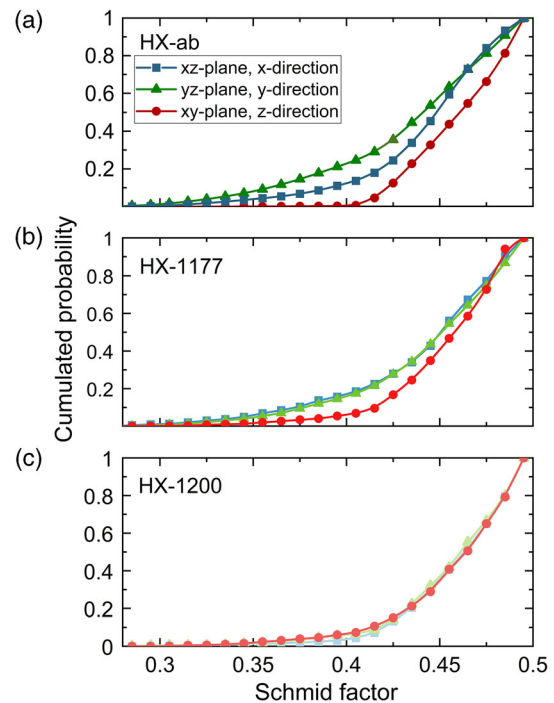
Figure 13. Distribution of Schmid factors of a) HX-ab, b) HX-1177 , and c) HX-1200 for the favorable {111}<110> slide system for a loading in *x*-, *y*-, and *z*-direction. The curves were obtained by EBSD data analysis.

factors on the favored {111}<110> slip system for each loading direction. Higher Schmid factors mean that lower externally applied tensile stresses are sufficient to initiate slip. In the as-built condition, the results of the tensile tests are in good accordance with the evaluation of the Schmid factors. As shown in Figure 13a, the as-built condition exhibits higher Schmid factors in the *x*-direction than in the *y*-direction. Therefore, according to Schmid's law ($\tau = m^*\sigma$), the lower YS in the *x*-direction can be

**ADVANCED
SCIENCE NEWS**

www.advancedsciencenews.com

**ADVANCED
ENGINEERING
MATERIALS**

www.aem-journal.com

Figure 14. Comparison of misorientation mappings of Hastelloy X in a) the as-built, b,c) heat-treated conditions to mappings of heat-treated d) IN718 and e) 316L indicating the different degrees of recrystallization. Regions colored blue are recrystallized. f) The ratio of the strain in *x*- and *y*-direction to the axial strain at fracture, representing the *x–y* anisotropy.

attributed to the texture. The *z*-direction shows mainly higher Schmid factors and thus an even lower strength.

The aforementioned nontextural reasons for the anisotropic mechanical behavior in SLM processed materials were only reported for the as-built microstructure. However, the texture slightly changes after the heat treatments in the case of Hastelloy X because they lead to partly recrystallization. Consequently, the Schmid factor distribution becomes similar in the different directions and the mechanical properties become more isotropic. This is shown by the tensile tests (Figure 12) and the reduced ovality of fractured samples (Figure 7). The cumulated probability of the Schmid factors reveals clearly that anisotropic mechanical properties are still present in the HX-1177 condition, while the HX-1200 condition shows isotropic mechanical properties.

5.2. Comparison of the Behavior of Hastelloy X, 316L, and IN718

The detailed studies on Hastelloy X in the as-built and two differently heat-treated conditions showed that the microstructural and mechanical anisotropy is reduced if heat treatments are conducted at sufficiently high temperatures which facilitate recrystallization. In IN718 and 316L, misorientation mappings (see **Figure 14**) revealed an unrecrystallized grain structure after the heat treatments at 960 and 1050 °C. However, the results of the ovality analysis seem to be contrary for IN718 because the heat treatment still leads to a lower ovality. As the calculation of the ovality is based on the ratio of the absolute diameters in *x*- and *y*-direction, this ratio depends on the ductility and the sample

geometry. However, the ratios of the transversal strain to the strain at fracture in the two transversal directions (ν_x and ν_y), which follows the calculation of the Poisson's ratio, are geometry independent. Thus, these values represent the transversal anisotropy in a better way than the geometry-based ovality (Figure 14f). These results are in good accordance with the fraction of recrystallization in all materials and conditions. IN718 exhibits similar strain ratios in the IN178-ab and IN718-960 condition because no recrystallization occurred during the heat treatment. In addition, heat-treated 316L exhibits a high deviation in ν_x and ν_y. In contrast, Hastelloy X exhibits a huge reduction of the *x–y* anisotropy with increasing heat treatment temperature due to an increasing amount of recrystallization.

Comparable with Hastelloy X, higher heat treatment temperatures above 1100 °C may also lead to recrystallization in SLM 316L,[45,46] but this will also go along with a loss in strength combined with a higher ductility[18,46] and a transformation of the fully austenitic microstructure to a duplex microstructure with low amounts of ferrite.[47] Diepold et al.[47] showed in earlier investigations the complex interaction of the different phases in the γ'/γ''-strengthened Ni-base superalloy IN718. It was found that ageing without prior solution heat treatments leads to an increase in strength due to strengthening by substructures and precipitates. The usually conducted solution heat treatment between 930 and 1050 °C will lead to recovery, but not to recrystallization and thus it can be assumed that anisotropic effects are still present.[48] Only at higher temperatures, partial (1100 °C) or full (1180 °C) recrystallization occurs,[49,50] which thus leads to a reduction of microstructural and mechanical anisotropy.[51]

**ADVANCED
SCIENCE NEWS**
www.advancedsciencenews.com

**ADVANCED
ENGINEERING
MATERIALS**
www.aem-journal.com

6. Conclusion

Selective laser melting along the gas flow direction may cause attenuation of the laser beam due to an insufficient removal of process by-products. To obtain stable processing parameters, a 67° rotating scan strategy is used in EOS M290 machines which skips an angular region. Consequently, the grain structure and texture are different in all three coordinate planes. Thus, unidirectional mechanical testing leads to oval cross sections of pulled tensile specimens. Schmid factors, calculated based on texture analysis, explain the higher (y-direction), medium (x-direction), and lower (z-direction) YS in the different directions of the as-built condition. Other influencing factors such as the grain shape and orientation of grain boundaries as well as melt pool boundaries may also be relevant for the anisotropy of mechanical properties, but are not considered as the main factors. Heat treatments above 1177 °C reduce the microstructural and mechanical anisotropy of Hastelloy X. No reduction of anisotropy was observed in IN718 and 316L because standard heat treatments were conducted at 960 and 1050 °C, i.e., below the recrystallization temperature. Generally, succeeding heat treatments reduce anisotropic effects if recrystallization occurs. However, the strength of the material decreases due to the vanishing of cell structures and the reduction of the dislocation density if no strengthening precipitates are formed.

Conflict of Interest

The authors declare no conflict of interest.

Data Availability Statement

Research data are not shared.

[1] D. Herzog, V. Seyda, E. Wycisk, C. Emmelmann, *Acta Mater.* **2016**, *117*, 371.

[2] E. Liverani, S. Toschi, L. Ceschini, A. Fortunato, *J. Mater. Process. Technol.* **2017**, *249*, 255.

[3] J. P. Kruth, L. Froyen, J. Van Vaerenbergh, P. Mercelis, M. Rombouts, B. Lauwers, *J. Mater. Process. Technol.* **2004**, *149*, 616.

[4] J.-P. Kruth, M. Badrossamay, E. Yasa, J. Deckers, L. Thijs, J. Van Humbeeck, in *16th Int. Symp. on Electromachining (ISEM XVI)*, SHANGHAI JIAO TONG UNIV PRESS, Shanghai, China, **2010**.

[5] N. T. Aboulkhair, N. M. Everitt, I. Ashcroft, C. Tuck, *Addit. Manuf.* **2014**, *1–4*, 77.

[6] Q. Jia, D. Gu, *J. Alloys Compd.* **2014**, *585*, 713.

[7] G. H. Cao, T. Y. Sun, C. H. Wang, Xing. Li, M. Liu, Z. X. Zhang, P. F. Hu, A. M. Russell, R. Schneider, D. Gerthsen, Z. J. Zhou, C. P. Li, G. F. Chen, *Mater. Charact.* **2018**, *136*, 398.

[8] M. Pröbstle, S. Neumeier, J. Hopfenmüller, L. P. Freund, T. Niendorf, D. Schwarze, M. Göken, *Mater. Sci. Eng. A* **2016**, *674*, 299.

[9] L. Thijs, F. Verhaeghe, T. Craeghs, J. Van Humbeeck, J.-P. Kruth, *Acta Mater.* **2010**, *58*, 3303.

[10] A. Keshavarzkermani, R. Esmaeilizadeh, U. Ali, P. D. Enrique, Y. Mahmoodkhani, N. Y. Zhou, A. Bonakdar, E. Toyserkani, *Mater. Sci. Eng. A* **2019**, *762*, 138081.

[11] S.-H. Sun, K. Hagihara, T. Nakano, *Mater. Des.* **2018**, *140*, 307.

[12] B. Cheng, S. Shrestha, K. Chou, *Addit. Manuf.* **2016**, *12*, 240.

[13] P. Mercelis, J.-P. Kruth, *Rapid Prototyping J.* **2006**, *12*, 254.

[14] X. Zhou, K. Li, D. Zhang, X. Liu, J. Ma, W. Liu, Z. Shen, *J. Alloys Compd.* **2015**, *631*, 153.

[15] L. Thijs, M. L. M. Sistiaga, R. Wauthle, Q. Xie, J.-P. Kruth, J. Van Humbeeck, *Acta Mater.* **2013**, *61*, 4657.

[16] M. Ni, C. Chen, X. Wang, P. Wang, R. Li, X. Zhang, K. Zhou, *Mater. Sci. Eng. A* **2017**, *701*, 344.

[17] T. Etter, K. Kunze, F. Geiger, H. Meidani, *IOP Conf. Ser. Mater. Sci. Eng.* **2015**, *82*, 012097.

[18] D. Tomus, Y. Tian, P. A. Rometsch, M. Heilmaier, X. Wu, *Mater. Sci. Eng. A* **2016**, *667*, 42.

[19] M. Tang, P. C. Pistorius, *JOM* **2017**, *69*, 516.

[20] K. Kunze, T. Etter, J. Grässlin, V. Shklover, *Mater. Sci. Eng. A* **2015**, *620*, 213.

[21] P. Hanzl, M. Zetek, T. Bakša, T. Kroupa, *Procedia Eng.* **2015**, *100*, 1405.

[22] G. E. Bean, T. D. McLouth, D. B. Witkin, S. D. Sitzman, P. M. Adams, R. J. Zaldivar, *J. Mater. Eng. Perform.* **2019**, *28*, 1942.

[23] D. Deng, R. L. Peng, H. Brodin, J. Moverare, *Mater. Sci. Eng. A* **2018**, *713*, 294.

[24] N. Uzan, I. Rosenthal, A. Stern, *Metallogr. Microstruct. Anal.* **2016**, *5*, 512.

[25] A. Mertens, S. Reginster, Q. Contrepois, T. Dormal, O. Lemaire, J. Lecomte-Beckers, *Mater. Sci. Forum* **2014**, *783–786*, 898.

[26] A. Ladewig, G. Schlick, M. Fisser, V. Schulze, U. Glatzel, *Addit. Manuf.* **2016**, *10*, 1.

[27] A. Masmoudi, R. Bolot, C. Coddet, *J. Mater. Process. Technol.* **2015**, *225*, 122.

[28] D. Wang, S. Wu, F. Fu, S. Mai, Y. Yang, Y. Liu, C. Song, *Mater. Des.* **2017**, *117*, 121.

[29] J. Reijonen, A. Revuelta, T. Riipinen, K. Ruusuvuori, P. Puukko, *Addit. Manuf.* **2020**, *32*, 101030.

[30] B. Ferrar, L. Mullen, E. Jones, R. Stamp, C. J. Sutcliffe, *J. Mater. Process. Technol.* **2012**, *212*, 355.

[31] O. Andreau, I. Koutiri, P. Peyre, J.-D. Penot, N. Saintier, E. Pessard, T. De Terris, C. Dupuy, T. Baudin, *J. Mater. Process. Technol.* **2019**, *264*, 21.

[32] J. Bamberg, G. Zenzinger, A. Ladewig, AIP Conference Proceedings, **2016**, *1650*, 156.

[33] Y.-A. Song, W. Koenig, *CIRP Ann.* **1997**, *46*, 127.

[34] L. N. Carter, C. Martin, P. J. Withers, M. M. Attallah, *J. Alloys Compd.* **2014**, *615*, 338.

[35] J. Liu, Q. Chen, Y. Zhao, W. Xiong, A. To, in *Proc. of the 9th Inter. Symp. on Superalloy 718 & Derivatives: Energy, Aerospace, and Industrial Applications* (Eds: E. Ott, X. Liu, J. Andersson, Z. Bi, K. Bockenstedt, I. Dempster, J. Groh, K. Heck, P. Jablonski,

2100622 (12 of 13)

M. Kaplan, D. Nagahama, C. Sudbrack), Springer International Publishing, Springer, Cham, **2018**, p. 749.

[36] R. Acharya, J. A. Sharon, A. Staroselsky, *Acta Mater.* **2017**, *124*, 360.

[37] J. Liu, A. C. To, *Addit. Manuf.* **2017**, *16*, 58.

[38] V. Ocelík, I. Furár, J. T.M. De Hosson, *Acta Mater.* **2010**, *58*, 6763.

[39] X. Liu, C. Zhao, X. Zhou, Z. Shen, W. Liu, *Mater. Des.* **2019**, *168*, 107677.

[40] N. J. Harrison, I. Todd, K. Mumtaz, *Acta Mater.* **2015**, *94*, 59.

[41] S. Clijsters, T. Craeghs, S. Buls, K. Kempen, J.-P. Kruth, *Int. J. Adv. Manuf. Technol.* **2014**, *75*, 1089.

[42] W. Shifeng, L. Shuai, W. Qingsong, C. Yan, Z. Sheng, S. Yusheng, *J. Mater. Process. Technol.* **2014**, *214*, 2660.

[43] S. Zhou, Y. Su, R. Gu, Z. Wang, Y. Zhou, Q. Ma, M. Yan, *Materials* **2019**, *12*, 73.

[44] A. A. Deev, P. A. Kuznetcov, S. N. Petrov, *Phys. Procedia* **2016**, *83*, 789.

[45] O. O. Salman, C. Gammer, A. K. Chaubey, J. Eckert, S. Scudino, *Mater. Sci. Eng. A* **2019**, *748*, 205.

[46] D. Kong, C. Dong, X. Ni, L. Zhang, J. Yao, C. Man, X. Cheng, K. Xiao, X. Li, *J. Mater. Sci. Technol.* **2019**, *35*, 1499.

[47] B. Diepold, N. Vorlaufer, S. Neumeier, T. Gartner, M. Göken, *IJMMM* **2020**, *27*, 640.

[48] M. L. Montero-Sistiaga, S. Pourbabak, J. Van Humbeeck, D. Schryvers, K. Vanmeensel, *Mater. Des.* **2019**, *165*, 107598.

[49] W. M. Tucho, P. Cuvillier, A. Sjolyst-Kverneland, V. Hansen, *Mater. Sci. Eng. A* **2017**, *689*, 220.

[50] W. M. Tucho, V. Hansen, *J. Mater. Sci.* **2019**, *54*, 823.

[51] N. Kouraytem, J. Varga, B. Amin-Ahmadi, H. Mirmohammad, R. A. Chanut, A. D. Spear, O. T. Kingstedt, *Mater. Des.* **2020**, 109228.